


## Pressure-driven electronic and structural phase transition in intrinsic magnetic topological insulator $\text{MnSb}_2\text{Te}_4$

Yunyu Yin,<sup>1,\*</sup> Xiaoli Ma ,<sup>1,\*</sup> Dayu Yan,<sup>1,2,\*</sup> Changjiang Yi,<sup>1</sup> Binbin Yue,<sup>3</sup> Jianhong Dai,<sup>1</sup> Lin Zhao,<sup>1</sup> Xiaohui Yu,<sup>1,2,4</sup> Youguo Shi,<sup>1,2,†</sup> Jian-Tao Wang,<sup>1,2,4,‡</sup> and Fang Hong<sup>1,2,4,§</sup>

<sup>1</sup>Beijing National Laboratory for Condensed Matter Physics and Institute of Physics, Chinese Academy of Sciences, Beijing 100190, China

<sup>2</sup>School of Physical Sciences, University of Chinese Academy of Sciences, Beijing 100190, China

<sup>3</sup>Center for High Pressure Science & Technology Advanced Research, Beijing 100094, China

<sup>4</sup>Songshan Lake Materials Laboratory, Dongguan, Guangdong 523808, China

**HPSTAR**  
1329-2021



(Received 27 July 2021; accepted 10 November 2021; published 29 November 2021)

Intrinsic magnetic topological insulators provide an ideal platform to achieve various exciting physical phenomena. However, this kind of materials and related research are still very rare. In this work, we reported the electronic and structural phase transitions in the intrinsic magnetic topological insulator  $\text{MnSb}_2\text{Te}_4$  driven by hydrostatic pressure. Electric transport results revealed that temperature dependent resistance showed a minimum value near short-range antiferromagnetic (AFM) ordering temperature  $T_N'$ , which declines with pressure. The short-range AFM ordering was sensitive to pressure and fully suppressed above 11.5 GPa. The intensity of three Raman vibration modes in  $\text{MnSb}_2\text{Te}_4$  declined quickly starting from 7.5 GPa and these modes become undetectable above 9 GPa, suggesting possible insulator-metal transition, which is further confirmed by theoretical calculation. *In situ* x-ray diffraction demonstrated that an extra diffraction peak appears near 9.1 GPa and  $\text{MnSb}_2\text{Te}_4$  started to enter an amorphouslike state above 16.6 GPa, suggesting the structural origin of suppressed AFM ordering and metallization. This work has demonstrated the correlation among interlayer interaction, magnetic ordering, and electric behavior, which could benefit the understanding of the fundamental properties of this kind of materials and devices.

DOI: [10.1103/PhysRevB.104.174114](https://doi.org/10.1103/PhysRevB.104.174114)

### I. INTRODUCTION

When magnetic ordering is introduced to topological insulators, they will display a lot of unusual physical properties, such as topological quantum behavior, Chern-insulator and axion-insulator phases, and so-called “intrinsic magnetic topological insulators” [1–4]. Previous works have already demonstrated that introducing magnetism into time-reversal-invariant topological insulators  $(\text{Bi}, \text{Sb})_2\text{Te}_3$  by Cr doping can achieve the quantum anomalous Hall effect (QAHE) [5–10]. However, such kinds of materials are still very rare. Recently,  $\text{MnBi}_2\text{Te}_4$  and  $\text{MnSb}_2\text{Te}_4$  have been synthesized in forms of single crystal and epitaxial film, and studied by a few groups [11–18], and they are expected to be robust intrinsic magnetic topological insulators since the magnetic contribution is from the magnetic atoms on lattice sites, not by element doping. And the QAHE has been realized by Deng *et al.* in odd-layered  $\text{MnBi}_2\text{Te}_4$  at 1.4 K without magnetic field and it can be enhanced to 6.5 K by external magnetic field [2], which helps to align all magnetic layers in ferromagnetic geometry. Gong *et al.* investigated MBE-grown  $\text{MnBi}_2\text{Te}_4$  films by superconducting quantum interference devices and

angle-resolved photoemission spectroscopy and observed the anisotropic magnetic behavior and the highly layer-number dependent behavior of electronic band structures [12]. The septuple layer shows archetypal Dirac-type energy bands with isotropic dispersion behavior and typical three-dimensional (3D) character, quite different from the warped surface state of pure  $\text{Bi}_2\text{Te}_3$  [12]. Shi *et al.* reported the magnetoresistance effect and anomalous hall effect (AHE) in mechanical exfoliated  $\text{MnSb}_2\text{Te}_4$ , and AHE can be observed until  $\sim 35$  K [15]. Wimmer *et al.* observed a two-dimensional Dirac cone in epitaxial Mn excess  $\text{MnSb}_2\text{Te}_4$  films with ultrahigh ferromagnetic ordering temperature at 45–50 K [18], further confirming the electronic properties of an intrinsic magnetic topological insulator.

$\text{MnBi}_2\text{Te}_4$  and  $\text{MnSb}_2\text{Te}_4$  are sister materials and form in the same structure (Fig. 1) at ambient conditions, while  $\text{MnBi}_2\text{Te}_4$  is an electron-carrier semiconductor and  $\text{MnSb}_2\text{Te}_4$  is a hole-carried semiconductor [18–23]. Both can be mechanically exfoliated by special procedure and the interlayer interaction is quite similar with the van der Waals interaction in  $\text{Bi}_2\text{Te}_3$ , which are sensitive to external strain effect [24,25]. External pressure could help to reveal the relation between interlayer interaction and fundamental properties [26–29], which is a benefit for effective controlling of their exotic properties and promoting the application in the field of multifunctional electronic devices. Pei *et al.* have done a systematic study on  $\text{MnBi}_2\text{Te}_4$  by using diamond anvil cell (DAC) [25], and found that it undergoes a

\*These authors contributed equally to this work.

†ygshi@iphy.ac.cn

‡wjt@iphy.ac.cn

§hongfang@iphy.ac.cn

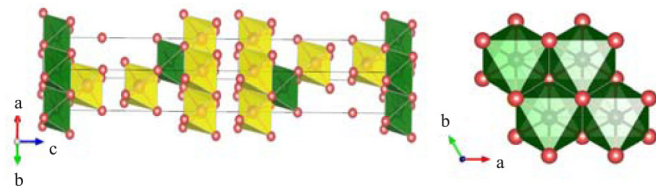


FIG. 1. The atomic structure of intrinsic magnetic topological insulator  $\text{MnSb}_2\text{Te}_4$ . The yellow octahedral is  $\text{SbTe}_6$  unit while green octahedral is  $\text{MnTe}_6$  unit.

metal-semiconductor-metal transition under high pressure and its antiferromagnetic (AFM) ordering is suppressed. A similar work was done by Chen *et al.* with a lower pressure range and displayed similar results [24]. The competition between bulk state and surface state is supposed to be responsible for the two step transitions on resistivity [25].

Since the carrier type in  $\text{MnSb}_2\text{Te}_4$  is different from  $\text{MnBi}_2\text{Te}_4$ , how the electronic properties respond to external pressure/strain is of great scientific interest [30–32]. In this work, we did a systematic study on  $\text{MnSb}_2\text{Te}_4$  under high pressure, based on electric transport, *in situ* Raman spectroscopy, synchrotron x-ray diffraction (XRD), and theoretical calculation.  $\text{MnSb}_2\text{Te}_4$  undergoes two phase transitions from original crystalline phase to an amorphouslike phase upon compression, and experience the semiconductor–poor metal–good metal transition, which is quite different from the phase change route observed in  $\text{MnBi}_2\text{Te}_4$ . There is a strong anisotropic behavior of out-of-plane Sb/Mn-Te interaction, revealed by the anisotropic compression behavior of two phonon modes. Meanwhile, the short-range antiferromagnetic ordering is suppressed with pressure and is finally destroyed near 11.5 GPa, which is quite consistent with the structural phase transition process. This work has demonstrated that the electronic behavior is totally different in these two systems with hole and electron carrier. Short-range spin ordering in  $\text{MnSb}_2\text{Te}_4$  could arouse strong scattering behavior on electric transport and it always exists until the phase transition, which provides a good platform to study the correlation behavior of spin and charge in intrinsic magnetic topological insulators.

## II. EXPERIMENT

The  $\text{MnSb}_2\text{Te}_4$  single crystals were synthesized via the flux method. High purity raw materials Mn (99.99%), Sb (99.9999%), and Te (99.9999%) were mixed in an Ar-filled glove box at a molar ratio of Mn : Sb : Te = 1 : 10 : 16. The mixture was placed in an alumina crucible and sealed in an evacuated quartz tube by a turbomolecular pump, which can generate a degree of vacuum  $\sim 10^{-3}$  Pa in the tube. The tube was heated to 700 °C for 10 h and dwelt for 20 h. Then, the tube was slowly cooled to 630 °C at a rate of 0.5 °C/h, followed by separation of the crystals from the flux by centrifugation. Large shiny crystals were obtained at the bottom of the crucible. A 300-micron culet DAC (BeCu) was used to produce a hydrostatic environment. A Re gasket was used as a support, *c*-BN epoxy mixtures were used as insulating materials, and KBr was used as the pressure medium. Pressure was determined by the *R1-R2* line shift of a ruby ball [33]. A thin and rectangular flake sample was placed in the

center of the chamber and the electric transport measurements were carried out in a standard four-probe geometry inside a Janis cryostat, which was cooled by a closed-loop  $\text{H}^4$  cycling system. *In situ* XRD data were collected with a wavelength of 0.6199 Å at Beamline 4W2 at the Beijing Synchrotron Radiation Facility. The high-pressure Raman spectra were collected using a LabRAM HR Evolution spectrometer and a 633-nm laser was used.

Our density functional theory (DFT) calculations were performed using the Vienna *ab initio* simulation package (VASP) [34] with the projector augmented wave method [35] and spin polarized generalized gradient approximation [36] for the exchange-correlation energy. The valence states  $3p^63d^64s^1$  for Mn,  $5s^25p^3$  for Sb, and  $5s^25p^4$  for Te were used with the energy cutoff of 500 eV for the plane wave basis set. To simulate the interlayer AFM coupling [22], an AFM rhombohedral primitive cell [21] was used with a van der Waals correction [37]. The Brillouin zone was sampled with a  $7 \times 7 \times 7$  Monkhorst-Pack special *k*-point grid. Throughout our calculations up to 15 GPa, the DFT + *U* method [38] was used with an effective value  $U_{\text{eff}} = 3$  eV for the Mn *3d* electrons. The geometries were optimized with symmetry constraints until the remaining atomic forces are less than  $10^{-2}$  eV/Å and the energy convergence criterion was set at  $10^{-8}$  eV. The electronic band structures and density of states were calculated by the modified Becke-Johnson (mBJ) functional [39] with the DFT + *U* method. The magnetic moments on Mn sites are calculated to be 4.42–4.45  $\mu_B$ , and the *3d* bands of Mn atoms are mainly located in an energy range between  $-5$  and  $-6$  eV below the Fermi level.

## III. RESULTS AND DISCUSSION

The electric transport measurement was carried out based on standard four-probe geometry [Fig. 2(a)]. Compared with the van der Pauw four-probe configuration, the standard four-probe configuration provides a higher liability and stability on transport data collecting. At low pressure,  $\sim 1.6$  GPa, the crystal shows metallic behavior above  $\sim 52$  K and then turns into a semiconducting state [as seen in Fig. 2(a)], which is quite consistent with the behavior of single crystal  $\text{MnSb}_2\text{Te}_4$  at ambient conditions [22]. This transition is assumed to associate with the short-range AFM correlation/ordering of Mn sublattice [22], while it shows a long-range AFM ordering transition near 19 K [22], 25 K [40], or 31 K [41] confirmed by the magnetic measurement. Recent work on epitaxial  $\text{MnSb}_2\text{Te}_4$  even shows a high  $T_c$  at 45–50 K [18]. The difference on the transition temperature of long-range spin ordering in  $\text{MnSb}_2\text{Te}_4$  indicates that the transition is sensitive to the site mixing, which cannot be well controlled during sample synthesis due to the close atomic size of Mn and Sb, and chemical stoichiometry as well [18]. By applying a magnetic field parallel to the *ab* plane, we found that the *M-H* curve of  $\text{MnSb}_2\text{Te}_4$  crystal almost has no hysteresis (see Fig. S1 of the Supplemental Material [42]), so our sample should be antiferromagnetic ordering, different from recent work about ferromagnetic ordering in Mn-rich  $\text{MnSb}_2\text{Te}_4$  [18]. As pressure increases, the temperature dependent resistance shows a monotonous decreasing trend until 16.5 GPa [Fig. 2(a)]. Meanwhile, we calculated the first derivative of

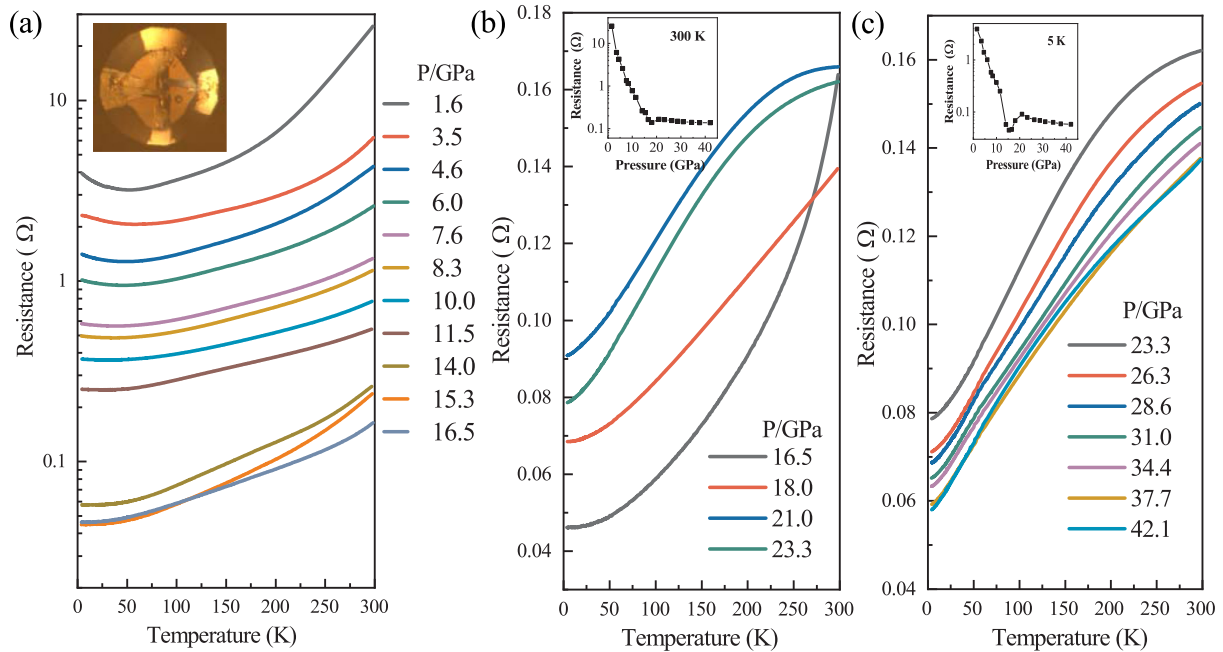


FIG. 2. The electric transport properties ( $R$ - $T$  curves) of  $\text{MnSb}_2\text{Te}_4$  crystal under high pressure. (a) Pressure up to 16.5 GPa, (b) up to 23.3 GPa, (c) up to 42.1 GPa; insets: (a) photograph of sample inside DAC chamber at 42.1 GPa, (b) the pressure dependent resistance at 300 K, (c) the pressure dependent resistance at 5 K.

the  $R$ - $T$  curve of  $\text{MnSb}_2\text{Te}_4$ , and obtained the trend of the short-range AFM ordering temperature with pressure: as the pressure increases, the kink becomes weaker, and it shifts towards lower temperature, accompanied by the suppression of magnetism, which was strongly suppressed near 10 GPa and becomes undetectable above 11.5 GPa, above which the sample shows complete metallic behavior over the entire temperature range. We define this kink as  $T_N'$ , and its trend can be seen in Fig. S2 in the Supplemental Material [42]. However, the sample resistance shows abnormal behavior between 16.5 and 21.0 GPa, during which the resistance at low temperature increases [Fig. 2(b)]. Starting from 21.0 GPa, the temperature dependent resistance shows a monotonous decreasing trend and does not change too much above 31.0 GPa [Fig. 2(c)]. For reference, the pressure dependent resistances (log scale) at 300 and 5 K are plotted in the insets in Figs. 2(b) and 2(c), respectively.

Compared with high pressure transport behavior of  $\text{MnBi}_2\text{Te}_4$  crystal [25],  $\text{MnSb}_2\text{Te}_4$  shows some similarity but there is also much different behavior. Pei *et al.* and Chen *et al.* have done a high pressure study on  $\text{MnBi}_2\text{Te}_4$  independently [24,25]; their high-pressure experiments both demonstrated the suppression of AFM behavior, which is to some extent similar to our current work. Previous studies demonstrate that  $\text{MnBi}_2\text{Te}_4$  shows typical AFM ordering [2,12,22], while  $\text{MnSb}_2\text{Te}_4$  shows antiferromagnetic or ferrimagnetic and even ferromagnetic ordering [18,41]. The ferrimagnetic behavior of  $\text{MnSb}_2\text{Te}_4$  is mainly due to the antisite behavior of Mn and Sb, which has been confirmed by neutron scattering experiment [40]. As mentioned above, in our work, the magnetic measurement shows that  $\text{MnSb}_2\text{Te}_4$  is almost antiferromagnetic at 5 K (Fig. S1 [42]). However, the transport behavior is totally different below this critical pressure. The resistance of  $\text{MnBi}_2\text{Te}_4$

increases with pressure up to 10.3 or 12.5 GPa [24,25], while the resistance of  $\text{MnSb}_2\text{Te}_4$  always decreases with pressure below 16.5 GPa. In addition, the original metallic state of  $\text{MnBi}_2\text{Te}_4$  at low pressure become a semiconducting state as pressure increases, and then turns back to a metallic state above 19 GPa [25].

In order to understand the underlying mechanism of the suppressed magnetism in  $\text{MnSb}_2\text{Te}_4$  and the electric transport anomaly upon compression, we did an *in situ* study on the static and dynamic structures by using synchrotron XRD and Raman spectroscopy, as presented in Fig. 3. Based on the XRD data under various pressures, we can observe a clear phase transition between 16.6 and 18.0 GPa, during which the intensity of most diffraction starts to become weaker and weaker [Fig. 3(a)]. The sample itself finally enters an amorphouslike phase upon further compression, as shown in Figs. S3 and S4 in the Supplemental Material [42]. Another small change is that there is new peak appearing starting at 9.1 GPa near  $2\theta \approx 15^\circ$ . All the other diffraction peaks of original phase are kept. To reveal the possible phase transition above 9.1 GPa, we did theoretical simulation to search possible new phases under high pressure. However, even when we relaxed the crystal lattice parameter and the stacking form of different layers, the final stable structure always went back to the original phase. Pei *et al.* did a systematic study on  $\text{MnBi}_2\text{Te}_4$  under high pressure and they only observed the amorphous transition and didn't find any extra anomaly at the low pressure range [25]. Hence, we speculate that the new peak could be contributed by a superstructure or local short-range ordering. A similar transition was also observed in  $\text{SnBi}_2\text{Te}_4$  [43]. Unfortunately, the accurate structure cannot be solved due to the low energy x-ray or short  $q$  range in the current work and in  $\text{SnBi}_2\text{Te}_4$  as well [43], and further work

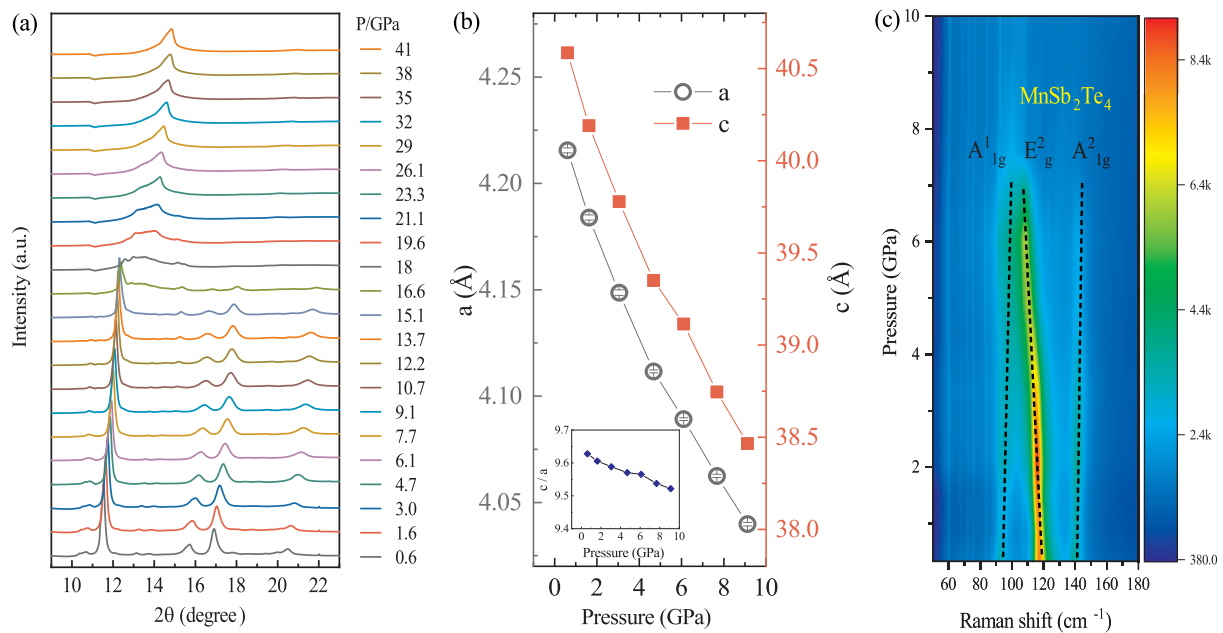


FIG. 3. High pressure structural behavior. (a) *In situ* x-ray diffraction (XRD): a small peak appears near  $2\theta = 15^\circ$ , starting from 9.1 GPa; near 18 GPa, the sample starts to transform to an amorphouslike state; (b) the lattice parameters up to 9.1 GPa; inset:  $c/a$  ratio, the change is very weak,  $c/a$  value at 9.1 GPa is only  $\sim 1\%$  smaller than that at 0.6 GPa; (c) micro-Raman spectroscopy: three vibration modes were observed; there is strong signal drop near 7.5 GPa and it is undetectable above 9 GPa; the mode near  $120\text{ cm}^{-1}$  shows negative compression behavior.

is still required to solve the fine structure above 9.1 GPa. The lattice parameters for the original  $R\bar{3}m$  phase obtained from XRD pattern refinement is presented in Fig. 3(b). The pressure dependent  $c/a$  ratio is shown in the inset of Fig. 3(b), and the change is quite small. At 9.1 GPa, the  $c/a$  ratio is only reduced by  $\sim 1\%$  compared with the value at 0.6 GPa, suggesting the isotropic compressibility of  $\text{MnSb}_2\text{Te}_4$ , though it is in the form of a layered structure. The raw data of lattice parameters was provided in Table S1 in the Supplemental Material [42].

To reveal the lattice dynamic behavior, Raman spectra were collected *in situ* inside DAC. Three vibration modes have been observed and the initial position of three modes are at  $\sim 92$ , 118, and  $140\text{ cm}^{-1}$  [Fig. 3(c)]. Upon compression, two of them shift to a higher wave number while the middle mode shows negative compression behavior. The intensity of all Raman modes becomes weak above 7.5 GPa and undetectable above 9.0 GPa. The mode at  $\sim 92\text{ cm}^{-1}$  is still a mysterious mode; Wang *et al.* had been assigned to a surface phonon mode ( $\sim 95\text{ cm}^{-1}$ ) [44], and Guo *et al.* claimed the effect of surface oxidation [45], Rodríguez-Fernández *et al.* found a peak of  $\sim 88\text{ cm}^{-1}$  in a Te cluster in  $\text{Bi}_2\text{Te}_3$  with rich Te content (which is similar to the  $\sim 95\text{ cm}^{-1}$ ) [46], and Mal *et al.* found a  $\sim 94\text{ cm}^{-1}$  mode in their calculation but did not provide detailed information about the origin of this mode [47]. In the work of Mal *et al.*, the  $\sim 94\text{ cm}^{-1}$  mode stayed at the same position with temperature, while other modes showed clear temperature dependence [47]. In Pei *et al.*'s work on  $\text{MnBi}_2\text{Te}_4$ , they did not observe any vibration mode near between 80 and  $100\text{ cm}^{-1}$  [25]. Hence, more theoretical work is required to explain the origin of the  $\sim 92\text{ cm}^{-1}$  in  $\text{MnSb}_2\text{Te}_4$ . The  $118\text{ cm}^{-1}$  mode is expected to be an IR-active mode ( $A_{1u}^1$  in bulk [47], but it has been activated by a symmetry break

(it may be due to the surface effect of laser penetration or the antisite effect of Mn and Sb) and observed by Raman spectroscopy as a  $E_g^2$ , corresponding to the out-of-plane vibration of Sb (and/or antisite Mn) and Te atoms. The  $118\text{ cm}^{-1}$  mode displays a pressure negative dependence behavior, which is rarely reported in layered materials. The  $142\text{ cm}^{-1}$  mode can be assigned to the  $A_{1g}^2$  mode [47], which corresponds to out-of-plane vibration of Sb (and/or antisite Mn) and Te atoms as well. The different pressure dependence behavior of 118 and  $142\text{ cm}^{-1}$  modes suggests that there is strong anisotropy interaction among out-of-plane Sb (and/or antisite Mn) and Te atoms. The anisotropic out-of-plane interaction observed by Raman spectroscopy is to some extent consistent with the magnetic anisotropy observed by Wimmer *et al.* [18], though the magnetic anisotropy is from the interlayer interaction between Mn and Sb.

Based on the structural information revealed by XRD, the changes of resistance are quite consistent with the structural evolution. The fully suppression of magnetic scattering on resistance is accompanied by a structural phase transition starting from  $\sim 9$  GPa. The anomaly in resistance measurement between 16.5 and 18.0 GPa should originate from the structural phase transition starting at 16.6 GPa. Further compression induces amorphouslike behavior while the resistance does not change too much anymore, especially for those above 25.5 GPa. The electronic band structures and density of states (DOS) are calculated by the modified Becke-Johnson (mBJ) functional [39]. The electronic band structures and the partial DOSs for Mn, Sb, and Te atoms are plotted in Fig. 4 at ambient conditions, 5 and 10 GPa. The total DOS under high pressure was presented in Fig. S5 [42]. The magnetic moments on Mn sites are calculated to be  $4.42\text{--}4.45\mu_B$ , and the  $3d$  bands of

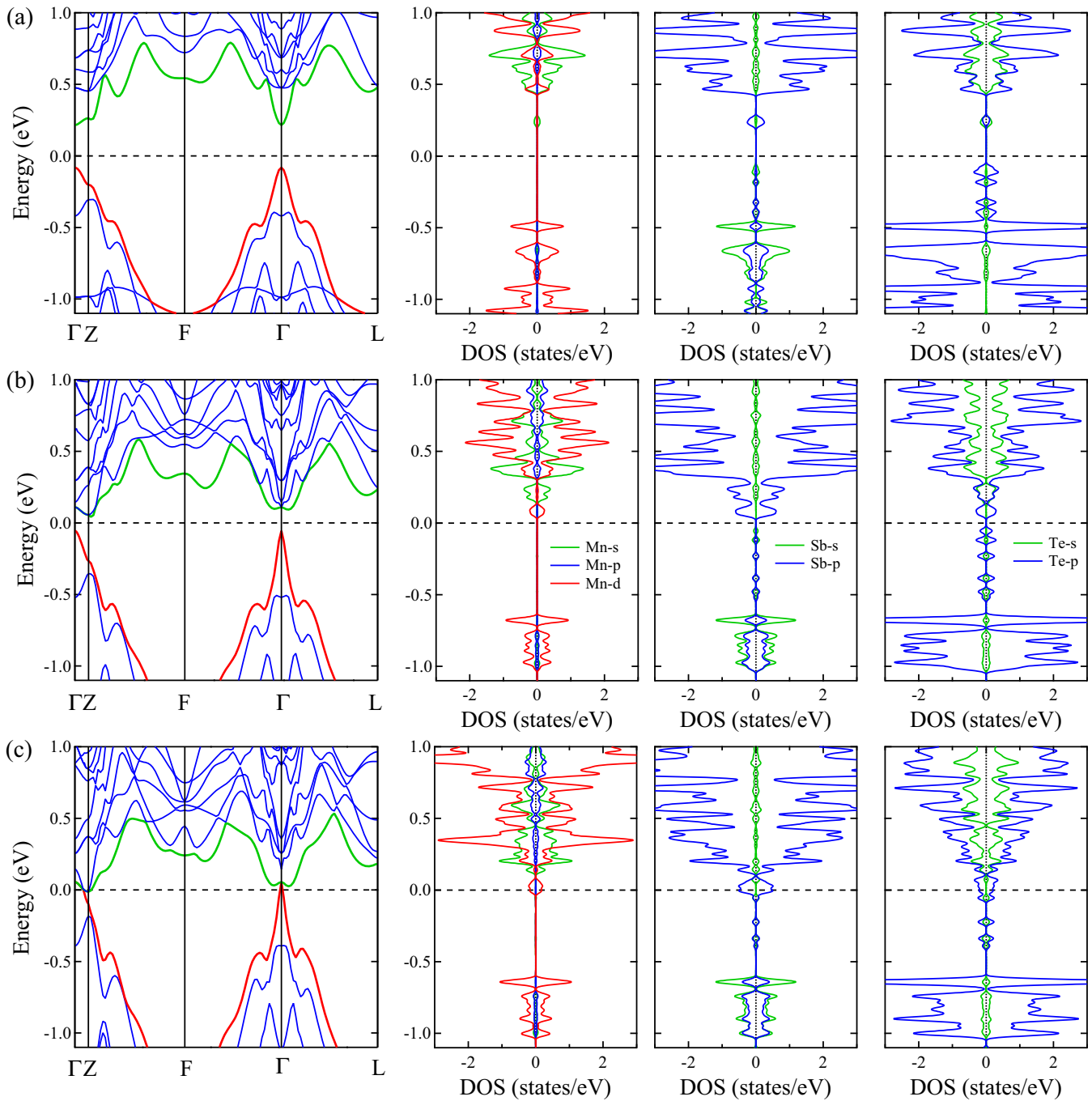


FIG. 4. Calculated electronic band structures and partial DOS of up spins and down spins for  $\text{MnSb}_2\text{Te}_4$  at (a) ambient condition ( $\sim 0$  GPa), (b) 5 GPa, and (c) 10 GPa using an AFM rhombohedral primitive cell. The lowest conduction band and highest valence band in band structures are marked with green and red lines, respectively. The direct band gap at ambient condition is 0.298 eV at  $\Gamma$  point. The  $3d$  bands of Mn atoms are mainly located in an energy range between  $-5$  and  $-6$  eV below the Fermi level and cannot be seen in this figure.

Mn atoms are mainly located in an energy range between  $-5$  and  $-6$  eV below the Fermi level. At ambient condition ( $\sim 0$  GPa),  $\text{MnSb}_2\text{Te}_4$  is a typical semiconductor with a direct band gap of 0.298 eV. The valence band maximum (VBM) and conduction band minimum (CBM) are located at the  $\Gamma$  point, as seen in Fig. 4(a), and the VBM is mainly contributed by Te- $p$  electrons, while the CBM is contributed by Sb- $p$  and Te- $sp$  electrons [see Fig. S5(a) [42]]. With an increase of pressure up to 5 GPa, it becomes an indirect band

gap semiconductor with a gap of 0.098 eV [see Fig. 4(b)]. The VBM is located at the  $\Gamma$  point and mainly contributed by Te- $p$  electrons, while the CBM is shifted along the Z- $F$  direction and mainly contributed by Sb- $p$  electrons and partial Te- $p$  and Mn- $d$  electrons [see Fig. S5(b)]. At 7 GPa, it has a small indirect band gap of 0.002 eV [see Fig. S5(c)]. Above 7 GPa, it becomes metallic, and the valence bands around the  $\Gamma$  point are crossing at the Fermi level. Under high pressure at 10 GPa, more valence and conduction bands are connected

around the Fermi level, as seen in Fig. 4(c), showing a strong metallic behavior with a peak of DOS at Fermi level [see Fig. S5(d)], and the states around the Fermi level are mainly contributed by the Sb-*p* (56%) and partial Te-*p* (24%) and Mn-*d* (20%) electrons. The calculation results are consistent with the Raman data, though the critical pressure points for metal-insulator transition is a little bit different by  $\sim 1$  GPa. As mentioned above, the Raman signal becomes extremely weak and even undetectable above 9.0 GPa, which is therefore due to the metallization of MnSb<sub>2</sub>Te<sub>4</sub>. Above 7.5 GPa, the Raman signal drops significantly and it should correspond to the appearance of “bad” metal state (as the band gap is just as close), compared with the “good” metal state above 9.0 GPa. A phase diagram was proposed based on the above measurement and discussion for reference, as seen in Fig. S6 in the Supplemental Material [42].

Besides the AFM behavior shown above, recently Wimmer *et al.* reported that Mn-rich MnSb<sub>2</sub>Te<sub>4</sub> is to be a ferromagnetic (FM) topological insulator [18]. To get a systematic understanding of the magnetic properties, we have further calculated the FM electronic band structures under 0, 3, 5, and 7 GPa (see Fig. S7 in the Supplemental Material [42]). At ambient conditions ( $\sim 0$  GPa), the FM MnSb<sub>2</sub>Te<sub>4</sub> has a direct band gap of 0.344 eV [see Fig. S7(a)]. The VBM and CBM are located at the  $\Gamma$  point related to the spin-down and spin-up bands, respectively, showing as a normal FM insulator as reported in Ref. [30]. With increasing pressure up to 3 GPa, the band gap is estimated to be of 0.125 eV [see Fig. S7(b)] along with the dropping of spin-down conduction band. Both VBM and CBM at the  $\Gamma$  point are related to the spin-down bands. With the dropping of spin-down conduction band, around 5 GPa, the valence and conduction bands cross at the Fermi level and form some nodes along the  $\Gamma Z$  and  $\Gamma F$  directions near the Fermi level [see Fig. S7(c)], showing as a topological Weyl semimetal as reported in Refs. [30,32]. Under 7 GPa, the valence and conduction bands are further crossed near the Fermi level [see Fig. S7(d)]. We can see that at the FM state, the band inversion can happen under pressure and induce a Weyl semimetal-insulator transition, however, the critical pressure point is largely shifted to a low value of  $\sim 5$  GPa, which is clearly inconsistent with our Raman data. The detailed topological properties including the nontrivial topological surface state have been reported in several previous studies [18,30–32] and are omitted here.

#### IV. CONCLUSION

In summary, we report the electric transport behavior and structural phase transition of intrinsic magnetic topological

insulator MnSb<sub>2</sub>Te<sub>4</sub> under high pressure up to  $\sim 42$  GPa. At ambient pressure, electric resistance measurement demonstrated that MnSb<sub>2</sub>Te<sub>4</sub> experiences a metal-semiconductor transition near 52 K, below which a short-range AFM ordering is expected to form and is responsible for the resistance anomaly. Strong suppression of the Raman signal above 7.5 GPa indicated the initiation of metallization and band gap close, which is supported by the theoretical calculation. Clear metallization behavior is expected to exist at  $\sim 10$  GPa by calculation, which is also consistent with the appearance of new structure and disappearance of any Raman signal above 9.1 GPa. It is also consistent with the full metallization above 11.5 GPa. The short-range AFM ordering was sensitive to pressure and fully suppressed above 11.5 GPa, and MnSb<sub>2</sub>Te<sub>4</sub> underwent another structural phase transition starting at 16.5 GPa and entered an amorphouslike state. This work shows that the hole-carrier dominated MnSb<sub>2</sub>Te<sub>4</sub> has a totally different electric behavior and phase transition route from the electron-carrier dominated MnBi<sub>2</sub>Te<sub>4</sub>. The anisotropic out-of-plane phonon modes is to some extent consistent with the reported magnetic anisotropy behavior, suggesting possible lattice-spin coupling. Current work provides an insight to show the correlation among interlayer interaction, magnetic ordering, and electronic behavior in this compound.

#### ACKNOWLEDGMENTS

This work was supported by the National Key Research and Development Program of China (Grants No. 2016YFA0401503, No. 2018YFA0305700, and No. 2020YFA0711502), the National Natural Science Foundation of China (Grants No. 11575288, No. 11974387, No. 12004416, No. 12004014, and No. 22090041), the Strategic Priority Research Program and Key Research Program of Frontier Sciences of the Chinese Academy of Sciences (Grants No. XDB33000000, No. XDB25000000, and No. QYZDBSSW-SLH013), and the Youth Innovation Promotion Association of Chinese Academy of Sciences under Grant No. Y202003. The synchrotron x-ray diffraction experiment was done at Beamline 4W2 at the Beijing Synchrotron Radiation Facility. Some instruments used in this study were built for the Synergic Extreme Condition User Facility.

F.H. conceived the project. D.Y.Y., C.J.Y., and Y.G.S. synthesized the crystal. Y.Y.Y. and X.L.M. did the resistance and Raman measurement. B.B.Y. and J.H.D. carried out the synchrotron x-ray diffraction experiment. J.T.W. did the theoretical calculation. F.H. loaded the samples for resistance, Raman, and synchrotron x-ray diffraction experiments, and wrote the manuscript. All authors joined the discussion and made comments/revisions on the manuscript.

- [1] R. S. K. Mong, A. M. Essin, and J. E. Moore, *Phys. Rev. B* **81**, 245209 (2010).
- [2] Y. Deng, Y. Yu, M. Z. Shi, Z. Guo, Z. Xu, J. Wang, X. H. Chen, and Y. Zhang, *Science* **367**, 895 (2020).
- [3] D. Zhang, M. Shi, T. Zhu, D. Xing, H. Zhang, and J. Wang, *Phys. Rev. Lett.* **122**, 206401 (2019).

- [4] J. Li, Y. Li, S. Du, Z. Wang, B.-L. Gu, S.-C. Zhang, K. He, W. Duan, and Y. Xu, *Sci. Adv.* **5**, eaaw5685 (2019).
- [5] R. Yu, W. Zhang, H.-J. Zhang, S.-C. Zhang, X. Dai, and Z. Fang, *Science* **329**, 61 (2010).
- [6] C.-Z. Chang, J. Zhang, X. Feng, J. Shen, Z. Zhang, M. Guo, K. Li, Y. Ou, P. Wei, and L.-L. Wang, *Science* **340**, 167 (2013).

- [7] J. G. Checkelsky, R. Yoshimi, A. Tsukazaki, K. S. Takahashi, Y. Kozuka, J. Falson, M. Kawasaki, and Y. Tokura, *Nat. Phys.* **10**, 731 (2014).
- [8] X. Kou, S. T. Guo, Y. Fan, L. Pan, M. Lang, Y. Jiang, Q. Shao, T. Nie, K. Murata, J. Tang, Y. Wang, L. He, T. K. Lee, W. L. Lee, and K. L. Wang, *Phys. Rev. Lett.* **113**, 137201 (2014).
- [9] A. J. Bestwick, E. J. Fox, X. Kou, L. Pan, K. L. Wang, and D. Goldhaber-Gordon, *Phys. Rev. Lett.* **114**, 187201 (2015).
- [10] J. Wang, B. Lian, and S.-C. Zhang, *Phys. Scr.* **2015**, 014003 (2015).
- [11] D. S. Lee, T.-H. Kim, C.-H. Park, C.-Y. Chung, Y. S. Lim, W.-S. Seo, and H.-H. Park, *CrystEngComm* **15**, 5532 (2013).
- [12] Y. Gong, J. Guo, J. Li, K. Zhu, M. Liao, X. Liu, Q. Zhang, L. Gu, L. Tang, X. Feng, D. Zhang, W. Li, C. Song, L. Wang, P. Yu, X. Chen, Y. Wang, H. Yao, W. Duan, Y. Xu, S.-C. Zhang, X. Ma, Q.-K. Xue, and K. He, *Chin. Phys. Lett.* **36**, 076801 (2019).
- [13] H. Li, S. Liu, C. Liu, J. Zhang, Y. Xu, R. Yu, Y. Wu, Y. Zhang, and S. Fan, *Phys. Chem. Chem. Phys.* **22**, 556 (2020).
- [14] C. Liu, Y. Wang, H. Li, Y. Wu, Y. Li, J. Li, K. He, Y. Xu, J. Zhang, and Y. Wang, *Nat. Mater.* **19**, 522 (2020).
- [15] G. Shi, M. Zhang, D. Yan, H. Feng, M. Yang, Y. Shi, and Y. Li, *Chin. Phys. Lett.* **37**, 047301 (2020).
- [16] M. M. Otrokov, I. P. Rusinov, M. Blanco-Rey, M. Hoffmann, A. Y. Vyazovskaya, S. V. Eremeev, A. Ernst, P. M. Echenique, A. Arnaud, and E. V. Chulkov, *Phys. Rev. Lett.* **122**, 107202 (2019).
- [17] J. Q. Yan, Q. Zhang, T. Heitmann, Z. Huang, K. Y. Chen, J. G. Cheng, W. Wu, D. Vaknin, B. C. Sales, and R. J. McQueeney, *Phys. Rev. Mater.* **3**, 064202 (2019).
- [18] S. Wimmer, J. Sánchez-Barriga, P. Küppers, A. Ney, E. Schierle, F. Freyse, O. Caha, J. Michalicka, M. Liebmann, and D. Primetzhofer, *Adv. Mater.* **33**, 2102935 (2021).
- [19] J. Cui, M. Shi, H. Wang, F. Yu, T. Wu, X. Luo, J. Ying, and X. Chen, *Phys. Rev. B* **99**, 155125 (2019).
- [20] S. H. Lee, Y. Zhu, Y. Wang, L. Miao, T. Pillsbury, H. Yi, S. Kempinger, J. Hu, C. A. Heikes, P. Quarterman, W. Ratcliff, J. A. Borchers, H. Zhang, X. Ke, D. Graf, N. Alem, C.-Z. Chang, N. Samarth, and Z. Mao, *Phys. Rev. Research* **1**, 012011 (2019).
- [21] M. M. Otrokov, I. I. Klimovskikh, H. Bentmann, D. Estyunin, A. Zeugner, Z. S. Aliev, S. Gass, A. U. B. Wolter, A. V. Koroleva, A. M. Shikin, M. Blanco-Rey, M. Hoffmann, I. P. Rusinov, A. Y. Vyazovskaya, S. V. Eremeev, Y. M. Koroteev, V. M. Kuznetsov, F. Freyse, J. Sanchez-Barriga, I. R. Amiraslanov *et al.*, *Nature (London)* **576**, 416 (2019).
- [22] J.-Q. Yan, S. Okamoto, M. A. McGuire, A. F. May, R. J. McQueeney, and B. C. Sales, *Phys. Rev. B* **100**, 104409 (2019).
- [23] A. Zeugner, F. Nietschke, A. U. B. Wolter, S. Gaß, R. C. Vidal, T. R. F. Peixoto, D. Pohl, C. Damm, A. Lubk, R. Hentrich, S. K. Moser, C. Fornari, C. H. Min, S. Schatz, K. Kißner, M. Ünzelmann, M. Kaiser, F. Scaravaggi, B. Rellinghaus, K. Nielsch *et al.*, *Chem. Mater.* **31**, 2795 (2019).
- [24] K. Y. Chen, B. S. Wang, J. Q. Yang, D. S. Parker, J. S. Zhou, Y. Uwatoko, and J. G. Cheng, *Phys. Rev. Mater.* **3**, 094201 (2019).
- [25] C. Pei, Y. Xia, J. Wu, Y. Zhao, L. Gao, T. Ying, B. Gao, N. Li, W. Yang, D. Zhang, H. Gou, Y. Chen, H. Hosono, G. Li, and Y. Qi, *Chin. Phys. Lett.* **37**, 066401 (2020).
- [26] W. Toyoshima, T. Masubuchi, T. Watanabe, K. Takase, K. Matsubayashi, Y. Uwatoko, and Y. Takano, *J. Phys.: Conf. Ser.* **150**, 042215 (2009).
- [27] C. R. S. Haines, M. J. Coak, A. R. Wildes, G. I. Lampronti, C. Liu, P. Nahai-Williamson, H. Hamidov, D. Daisenberger, and S. S. Saxena, *Phys. Rev. Lett.* **121**, 266801 (2018).
- [28] M. J. Coak, D. M. Jarvis, H. Hamidov, C. R. S. Haines, P. L. Alireza, C. Liu, S. Son, I. Hwang, G. I. Lampronti, D. Daisenberger, P. Nahai-Williamson, A. R. Wildes, S. S. Saxena, and J. G. Park, *J. Phys.: Condens. Matter* **32**, 124003 (2020).
- [29] R. A. Evarestov and A. Kuzmin, *J. Comput. Chem.* **41**, 1337 (2020).
- [30] L. Zhou, Z. Tan, D. Yan, Z. Fang, Y. Shi, and H. Weng, *Phys. Rev. B* **102**, 085114 (2020).
- [31] P. Li, J. Yu, Y. Wang, and W. Luo, *Phys. Rev. B* **103**, 155118 (2021).
- [32] H. Zhang, W. Yang, Y. Wang, and X. Xu, *Phys. Rev. B* **103**, 094433 (2021).
- [33] H. K. Mao, J. Xu, and P. M. Bell, *J. Geophys. Res.* **91**, 4673 (1986).
- [34] G. Kresse and J. Furthmüller, *Phys. Rev. B* **54**, 11169 (1996).
- [35] P. E. Blöchl, *Phys. Rev. B* **50**, 17953 (1994).
- [36] J. P. Perdew, K. Burke, and M. Ernzerhof, *Phys. Rev. Lett.* **77**, 3865 (1996).
- [37] A. Tkatchenko and M. Scheffler, *Phys. Rev. Lett.* **102**, 073005 (2009).
- [38] V. I. Anisimov, J. Zaanen, and O. K. Andersen, *Phys. Rev. B* **44**, 943 (1991).
- [39] A. D. Becke and E. R. Johnson, *J. Chem. Phys.* **124**, 221101 (2006).
- [40] T. Murakami, Y. Nambu, T. Koretsune, G. Xiangyu, T. Yamamoto, C. M. Brown, and H. Kageyama, *Phys. Rev. B* **100**, 195103 (2019).
- [41] D. Y. Yan, M. Yang, P. B. Song, Y. T. Song, C. X. Wang, C. J. Yi, and Y. G. Shi, *Phys. Rev. B* **103**, 224412 (2021).
- [42] See Supplemental Material at <http://link.aps.org/supplemental/10.1103/PhysRevB.104.174114> for more details on analyses for magnetic measurement, structure analysis, proposed phase diagram and theoretical calculations. The Supplemental Material includes Refs. [30,32].
- [43] R. Vilaplana, J. A. Sans, F. J. Manjón, A. Andrada-Chacón, J. Sánchez-Benítez, C. Popescu, O. Gomis, A. L. J. Pereira, B. García-Domene, P. Rodríguez-Hernández, A. Muñoz, D. Daisenberger, and O. Oeckler, *J. Alloys. Compd.* **685**, 962 (2016).
- [44] C. Wang, X. Zhu, L. Nilsson, J. Wen, G. Wang, X. Shan, Q. Zhang, S. Zhang, J. Jia, and Q. Xue, *Nano Res.* **6**, 688 (2013).
- [45] J.-H. Guo, F. Qiu, Y. Zhang, H.-Y. Deng, G.-J. Hu, X.-N. Li, G.-L. Yu, and N. Dai, *Chin. Phys. Lett.* **30**, 106801 (2013).
- [46] C. Rodríguez-Fernández, C. V. Manzano, A. H. Romero, J. Martín, M. Martín-González, M. Morais de Lima Jr., and A. Cantarero, *Nanotechnology* **27**, 075706 (2016).
- [47] P. Mal, G. Bera, G. R. Turpu, S. K. Srivastava, A. Gangan, B. Chakraborty, B. Das, and P. Das, *Phys. Chem. Chem. Phys.* **21**, 15030 (2019).